Results in Surfaces and Interfaces 18 (2025) 100415

Contents lists available at ScienceDirect

Results in Surfaces and Interfaces

journal homepage: www.elsevier.com/locate/rsurfi

Mixing enthalpy-driven variations in ablation thresholds and laser-induced crater morphologies of $CoCuFeNiMnMo_x$ (x=0.5, 1.0, 1.5) high-entropy alloys under UV nanosecond laser pulses

Hossein Mahdavi [a], Abdullah Kepçeoğlu [b], Armin Asghari Alamdari [a], Uğur Ünal [b,c], Hadi Jahangiri [b,*]

[a] Materials Science and Engineering, Koç University, Sariyer, 34450, Istanbul, Turkey
[b] Koç University Surface Science and Technology Center (KUYTAM), Koç University, Sariyer, 34450, Istanbul, Turkey
[c] Department of Chemistry, Koç University, Sariyer, 34450, Istanbul, Turkey

ARTICLE INFO

Keywords:
Laser
Ablation thresholds fluence
High-entropy alloy
Nanosecond laser

ABSTRACT

This study investigates the ablation threshold fluence and power dependence of ablation process in $CoCuFeNiMnMo_x$ (x = 0.5, 1.0, and 1.5) high-entropy alloys under ultraviolet nanosecond laser pulses. The ablation threshold value, a critical parameter determining the minimum energy density required for laser material removal, is explored in-depth. Mixing enthalpy, characterizing the energy change during the formation of solid solutions, is calculated for the alloys, shedding light on their atomic interactions and phase stability. Laser-induced crater morphologies are analyzed using white light interferometry and optical microscopy, showing distinct features influenced by laser fluence and pulse number. Results demonstrate that an increase in laser pulse energy correlates with an increase in standard deviation. The relationship between crater size, laser pulse energy, and ablation depth is examined, highlighting the alloys' diverse ablation thresholds.

1. Introduction

The research community has shown significant interest in the design and production of high-entropy alloys (HEAs) ever since the introduction of the equiatomic multicomponent alloy concept (Miracle and Senkov, 2017; Gao et al., 2016). Unlike traditional alloys, HEAs are comprised of at least five elements, each with a concentration ranging from 5 to 35 at%. The design of HEAs is commonly guided by four key concepts: high configurational entropy, sluggish diffusion kinetics, severe lattice distortion, and the cocktail effect (Miracle and Senkov, 2017; Gao et al., 2016; Pickering and Jones, 2016; Yeh, 2015). These materials, known for their diverse mechanical, electrochemical, magnetic, thermal, and anticorrosion properties, find applications across various fields utilized in different forms such as bulk materials, powders, and films (Zhang et al., 2014; Ma et al., 2015; Meghwal et al., 2020; Mahdavi et al., 2024).

Bulk samples, distinguished by properties such as high hardness and resistance to abrasion etc. and implemented as mechanical components or protective shields against oxidation or corrosion, can be manufactured through processes such as casting or spark plasma sintering (Jahangiri et al., 2021; Chen et al., 2013). Powdered HEAs are employed in many different applications such as electrocatalysis, sensing, and photothermal therapy, and their production methods include laser ablation, mechanical alloying. etc (Boulmer-Leborgne et al., 2010; Jahangiri et al., 2023; Song et al., 2024; Asghari Alamdari et al., 2024). HEA-coated films could serve as electrodes in electrochemical or photoelectrochemical applications, prepared through methods such as sputtering or Pulsed Laser Deposition (PLD) (Cropper, 2018; Guo et al., 2022). When using lasers to generate nano-powders or fabricating coating layers, it is essential to consider the materials' ablation threshold.

During the laser ablation process, the material surface is exposed to laser radiation, causing it to heat up, melt, and eventually evaporate (Martínez-Carmona and Vallet-Regí, 2020). UV lasers are often preferred for triggering ablation due to their distinct advantages over other types of lasers. Direct laser ablation, occurring over a few nanoseconds, is the primary mechanism responsible for material removal when using a UV laser. In contrast, with an IR laser, the formation of plasma can shield the laser radiation, limiting direct laser ablation and increasing the plasma temperature. This leads to an increased selective

* Corresponding author.
E-mail address: hjahangiri@ku.edu.tr (H. Jahangiri).

https://doi.org/10.1016/j.rsurfi.2025.100415
Received 11 November 2024; Received in revised form 30 December 2024; Accepted 5 January 2025
Available online 8 January 2025
2666-8459/© 2025 The Authors. Published by Elsevier B.V. This is an open access article under the CC BY-NC-ND license (http://creativecommons.org/licenses/by-nc-nd/4.0/).

removal of material by the plasma rather than through direct ablation (Preuss et al., 1995). The ablation process with UV lasers is predominantly photochemical rather than photothermal. This minimizes thermal effects, allowing for highly precise ablation with minimal heat-affected zones (HAZ) and reducing the risk of thermal damage. As a result, UV laser ablation preserves the structural integrity of the material, which is essential in applications requiring high precision (Liu et al., 1997). The shorter wavelength of UV lasers allows for a smaller focal spot size, thus the crater size is closer to the beam radius, enhancing spatial resolution and enabling cleaner cuts, smoother surfaces, and finer details. This higher precision makes UV lasers ideal for micro- and nano-fabrication applications where surface quality is crucial (Preuss et al., 1995; Assonov et al., 2009). UV lasers exhibit much higher reproducibility in the plasma emission. The combination of minimized thermal damage, high precision, and better reproducibility makes UV lasers suitable for the ablation of metals and alloys. The minimum energy required for this process, known as the ablation threshold energy, is influenced by various factors such as the laser wavelength, the surface morphology, the duration of the laser pulses, and the laser pulse energy (Martínez-Carmona and Vallet-Regí, 2020; Shih et al., 2020). This phenomenon is especially interesting when studying HEAs, a relatively new generation of materials composed of numerous elements arranged in unique structures. In recent years, these alloys have attracted considerable interest owing to their unique properties and promising range of applications (Redka et al., 2021; Pérez Blanes et al., 2023). When laser rays interact with a material, they can create craters on the surface. The relationship between the diameter and depth of these craters is influenced not only by the material composition but also by factors such as the number of laser pulses, laser power, laser wavelength, and other relevant parameters applied during the process (Wang et al., 2022; Mustafa et al., 2019; Takayama et al., 2018). Understanding these interactions is crucial for tailoring laser ablation processes to achieve desired outcomes in materials processing and modification. Ongoing research in this field has mostly focused on understanding the ablation thresholds of CoCuFeNiMnMo$_x$ (x = 0.5, 1.0, and 1.5) HEAs and the underlying mechanisms governing their removal. CoCuFeNiMnMo$_x$ (x = 0.5, 1.0, and 1.5) materials are promising candidates for catalytic applications, such as Hydrogen Evolution Reaction (HER) and Oxygen Evolution Reaction (OER) (Asghari Alamdari et al., 2024). The potential for these alloys to serve as effective catalysts in these reactions is an important aspect of their study. Furthermore, the ability to achieve nanoscale catalysts with high performance is crucial for these applications. Therefore, understanding the ablation thresholds of these materials is particularly valuable. This knowledge facilitates the use of liquid laser ablation techniques to synthesize nano powders, which can significantly enhance the performance of the catalysts in HER and OER applications. By studying the CoCuFeNiMnMo$_x$ (x = 0.5, 1.0, and 1.5) compositions, the aim is to optimize the laser parameters for effective nano powder synthesis and improve the catalytic efficiency in practical applications. This approach highlights the practical significance of the research in advancing the field of catalysis. Despite the promising properties of CoCuFeNiMnMo$_x$ (x = 0.5, 1.0, and 1.5) alloys, there is limited literature focusing on their laser processing behavior. By selecting this specific system, our study aims to fill this knowledge gap and contribute new insights into the laser-material interactions of HEAs. Understanding the fluence and power dependence of the ablation process in CoCuFeNiMnMo$_x$ (x = 0.5, 1.0, and 1.5) HEAs are crucial for advancing their respective nanopowders and nanoporous thin films (PLD coatings) with very fine dimensions to increase the specific surface area for applications in catalysis and surface engineering (Mahdavi et al., 2024; Tahir et al., 2024). Specifically, by correlating these parameters with the resulting crater dimensions and material removal efficiency, it is possible to optimize laser parameters for synthesizing nanoscale catalysts with enhanced performance for the Hydrogen Evolution Reaction (HER) and Oxygen Evolution Reaction (OER). Additionally, precise control of the ablation process can be leveraged for creating microscale features in advanced sensing or photothermal devices, expanding the functional versatility of these HEAs.

In this investigation, a laser with a nanosecond pulse duration and a wavelength of 340 nm is employed to examine the ablation thresholds of CoCuFeNiMnMo$_x$ (x = 0.5, 1.0, and 1.5) HEAs. The study specifically explores the impact of the number of laser pulses, laser pulse energy, and alloy composition on the depth, width, and morphology of the resulting craters. This study investigates the optimization of pulsed laser ablation process for HEAs for the first time, aiming to further progress the pulsed laser ablation and pulsed laser deposition techniques for rapid nanoparticle and nano-porous thin film production.

2. Experimental

In this investigation, cylindrical-shaped CoCuFeNiMnMo$_x$ (x = 0.5, 1.0, and 1.5) HEAs with a 10 mm diameter and 5 mm thickness served as targets. The surfaces of CoCuFeNiMnMo$_x$ (x = 0.5, 1.0, and 1.5) HEAs targets were prepared under identical conditions. The studied areas of the three targets underwent a six-stage grinding process using sandpaper with six different grit sizes (100, 300, 600, 800, 1000, and 2500), followed by polishing with 0.3 μm Al_2O_3 suspension. The impact of three available compositions of HEA was examined by subjecting them to a 340 nm laser. The study involved analyzing the shape, morphology, and dimensions of the laser induced crater, specifically focusing on depth and diameter, following varying numbers of laser pulses (1, 10, 100, and 1000) on the surfaces of CoCuFeNiMnMo$_x$ (x = 0.5, 1.0, and 1.5) HEAs targets. For all measurements, ten data points were recorded, and the average along with the standard deviation of the results was reported.

For this purpose, a Q-switched Nd:YAG laser with an integrated single-pass amplifier (Spectra-Physics Quanta-Ray, USA) system was employed. To generate the required laser wavelength, an OPO (Spectra-Physics primoScan/ULD, USA) was used, operating at a wavelength of 340 nm. The laser functioned at a repetition rate of 10 Hz, delivering an approximate pulse energy of 20 mJ with 10 ns pulse width. To ensure precise targeting of the laser beam a plano-convex lens with a 7 cm focal length was used to focus the laser onto the target material. The target was positioned by using micrometer resolution translation stages. The experimental setup, schematics, and lens focusing on the HEA target are depicted in Fig. 1. Surface morphology and crater features were examined using optical microscopy (OM) and white light interferometry (WLI). The depth of the crater after 1, 10, 100, and 1000 pulses was measured using a 2-D contact profilometer (DEKTAK 6 M, Bruker, USA).

Ablation threshold fluence values have been presented experimentally by using zero damage measurement method for the nanosecond laser pulses (Lednev et al., 2015), picosecond laser pulses (Liu, 1982), and femtosecond laser pulses (Lenzner et al., 2000) by various studies. In this method, the squared values of the crater diameter induced by material removal from the sample surface are plotted vs. laser fluence value. Zero damage is determined by calculating the slope of this plot using the following Equation (1). The ablation threshold fluence value is established at the point where this plot intersects the fluence axis.

$$D^2 = 2\omega^2 \ln\left(\frac{F}{F_{th}}\right) \tag{1}$$

In this equation, ω is the focused laser spot size (the radius of the focused laser spot) on the sample surface, F_{th} ablation threshold fluence value,

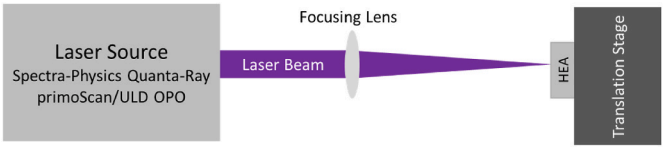


Fig. 1. The experimental setup schematics, including the laser beam, focusing lens, HEA target, and target translation stage.

and F is the laser fluence.

Table 1 displays seven different applied laser pulse energy levels of the nanosecond laser with a wavelength of 340 nm, along with their respective standard deviations for each measured power and the corresponding calculated laser fluence of the focused beam on the sample surface (Sharkov and Scrivens, 2005). It is evident from the table that an increase in pulse energy results in a corresponding increase in the standard deviation of the utilized laser pulse energy.

3. Results and discussion

Mixing enthalpy in HEAs refers to the energy change associated with the mixing of different elements at the atomic level to form a solid solution. It quantifies the heat absorbed or released when dissimilar atoms combine to form an alloy. This enthalpy characterizes the energetic interactions between dissimilar atoms, influencing the alloy's phase stability, microstructure, and properties. A higher mixing enthalpy suggests stronger atomic interactions, potentially leading to better phase stability (Ye et al., 2016; Guo et al., 2011). Mixing enthalpy can be calculated by Equation (2).

$$\Delta H_{mix} = \sum_{i=1\, j\neq 1}^{n} 4\, \Delta H_{ij}^{mix}\, ci\, cj \tag{2}$$

Where ΔH_{ij}^{mix} represents the enthalpy of mixing, and c_i indicates the atomic fraction of the binary liquid between the ith and jth elements.

The calculated mixing enthalpy values for three compositions are presented in Table 2. The $CoCuFeNiMnMo_{0.5}$ sample exhibits the highest mixing enthalpy at 132.2 J/mol, indicating stronger atomic bonds. Conversely, the $CoCuFeNiMnMo_{1.5}$ shows the lowest mixing enthalpy at 94.67 J/mol, suggesting weaker atomic bonds, potentially resulting in a HEA with reduced bond strength.

This study examines the single and multiple-pulse laser ablation threshold of $CoCuFeNiMnMo_x$ (x = 0.5, 1.0, and 1.5) HEAs at a nanosecond laser pulse duration, focusing on its pulse energy dependence. To explore the impact of varying laser pulse energy levels on laser-induced craters, the morphologies of the laser ablated craters are analyzed using WLI. The characteristics of the craters are influenced by the applied laser fluence level and the number of laser pulses at the same location. Generally, both the diameter and depth of the craters increase as the fluence and/or the number of pulses rise(Mustafa et al., 2019). Fig. 2 displays the crater morphology following the initial pulse burst, with the lowest pulse energy setting used (0.7 mJ, 1618 J/cm^2). While surface features are consistently observed under our experimental conditions, the degree of surface alteration is significantly influenced by the applied fluence and/or number of laser pulses. When employing the lowest pulse energy and the fewest pulses, spherical-tipped jets predominate at the center of the crater. This behavior suggests a 'foaming' effect on the molten surface, resulting in intricate structures such as jets and protrusions, a phenomenon elucidated by Ionin et al. and Mustafa et al. (Mustafa et al., 2018, 2019; Ionin et al., 2017).

The topographical morphology of the HEA $CoCuFeNiMnMo_x$ (x = 0.5, 1.0, and 1.5) was investigated under a wide range of laser pulse energies, ranging from 0.67 mJ to 11.92 mJ, utilizing WLI and OM. In Fig. 3, the topographical morphology resulting from laser irradiation at 11.92 mJ on the HEA $CoCuFeNiMnMo_x$ (x = 0.5, 1.0, and 1.5) is presented, with analysis conducted via WLI and OM. The figures depicting the results of laser effects at the remaining six power levels can be found in Figures S-1 and S-2 for WLI and OM, respectively. This observed morphology was categorized into three distinct regimes based on the Mo variation: $CoCuFeNiMnMo_{0.5}$, $CoCuFeNiMnMo_{1.0}$, and $CoCuFeNiMnMo_{1.5}$.

Table 2
The calculated mixing enthalpies of the $CoCuFeNiMnMo_x$ (x = 0.5, 1.0, and 1.5) HEAs.

	$CoCuFeNiMnMo_{0.5}$	$CoCuFeNiMnMo_{1.0}$	$CoCuFeNiMnMo_{1.5}$
ΔH_{mix} (J/mol)	132.20	111.10	94.67

At low fluence regime, the craters appear disc-shaped, and they transition to a more splash-dominated morphology as the applied laser pulse energy increases. Notably, within the range of the investigated parameters, no 'melt-free' crater was detected. As indicated by H. Mustafa et al. , it's evident that both the maximum depth (h) and diameter (d) of the craters expand with increasing laser pulse energy (Mustafa et al., 2018; Yalçın et al., 2008). The affected craters consists of two distinct regions: the first one is the inner zone, which has gone through melting and deepening, and the second region is one formed by the solidification of the molten inner zone and recast region, resembling a surrounding wall (Jing et al., 2023). According to the WLI and OM figures, it is recognized that the inner zone has expanded by increasing the applied pulse energy and simultaneously the radius and the number of surrounded wall (Yalçın et al., 2008).

Fig. 4 depicts the correlation between the rate of reduction in crater size increment and the increasing applied laser pulse energy for the $CoCuFeNiMnMo_x$ (x = 0.5, 1.0, and 1.5) alloys. It is shown that the squared crater diameter increases linearly with the logarithm of the laser fluence according to the following eqautions $CoCuFeNiMnMo_x$ (x = 0.5, 1.0, and 1.5) alloys, respectively.

$$y = 2628.8\, log\ \ x - 2305.8 \quad R^2 = 0.9235 \tag{3}$$

$$y = 3501.9\, log\ \ x - 5010.3 \quad R^2 = 0.9654 \tag{4}$$

$$y = 6599.4\, log\, x - 14664 \quad R^2 = 0.9897 \tag{5}$$

It reveals a parabolic increase in crater radius as laser power rises, with the rate of radius growth decreasing as power increases. Notably, the highest post-ablation crater radius is associated with $CoCuFeNiMnMo_{1.5}$, while the lowest is observed in $CoCuFeNiMnMo_{0.5}$. Thus, it was anticipated that the sample with the highest mixing enthalpy would have the highest ablation threshold, resulting in the smallest crater. This aligns well with the findings presented in Fig. 4, demonstrating that the ablation threshold decreases with the increase in Mo ratio and the reduction in mixing enthalpy values.

Fig. 5 depicts the correlation between the depth of the crater and the applied laser pulse energy for the $CoCuFeNiMnMo_x$ (x = 0.5, 1.0, and 1.5) alloys. Fig. 5 presents the relationship between the average crater depth and laser pulse energy. Notably, this relationship exhibits a quasi-linear trend on a logarithmic scale for all composition of the HEA, covering a laser power range up to 11.92 mJ. The semi-logarithmic equations relating crater depth to laser fluence for $CoCuFeNiMnMo_x$ (x = 0.5, 1.0, and 1.5) alloys are shown in the following equations, respectively.

$$y = 0.3701\, log\, x - 1.104 \quad R^2 = 0.9293 \tag{6}$$

Table 1
Applied laser pulse energy values of nanosecond laser pulses with 340 nm wavelength and focused laser beam fluence values.

	1	2	3	4	5	6	7
Laser pulse energy (mJ)	0.67	0.96	1.27	1.91	3.06	5.31	11.92
Standard deviation	±0.027	±0.0s86	±0.074	±0.085	±0.174	±0.346	±0.421
Fluence (J/cm^2)	1618.94	2319.68	3068.74	4615.19	7393.97	12830.72	28802.67



Fig. 2. Optical microscope images of laser induced surface structure patterns on the CoCuFeNiMnMo$_x$ a) x = 0.5, b) x = 1.0, and c) x = 1.5) after the initial single pulse exposure at 0.7 mJ (1618.94 J/cm^2).

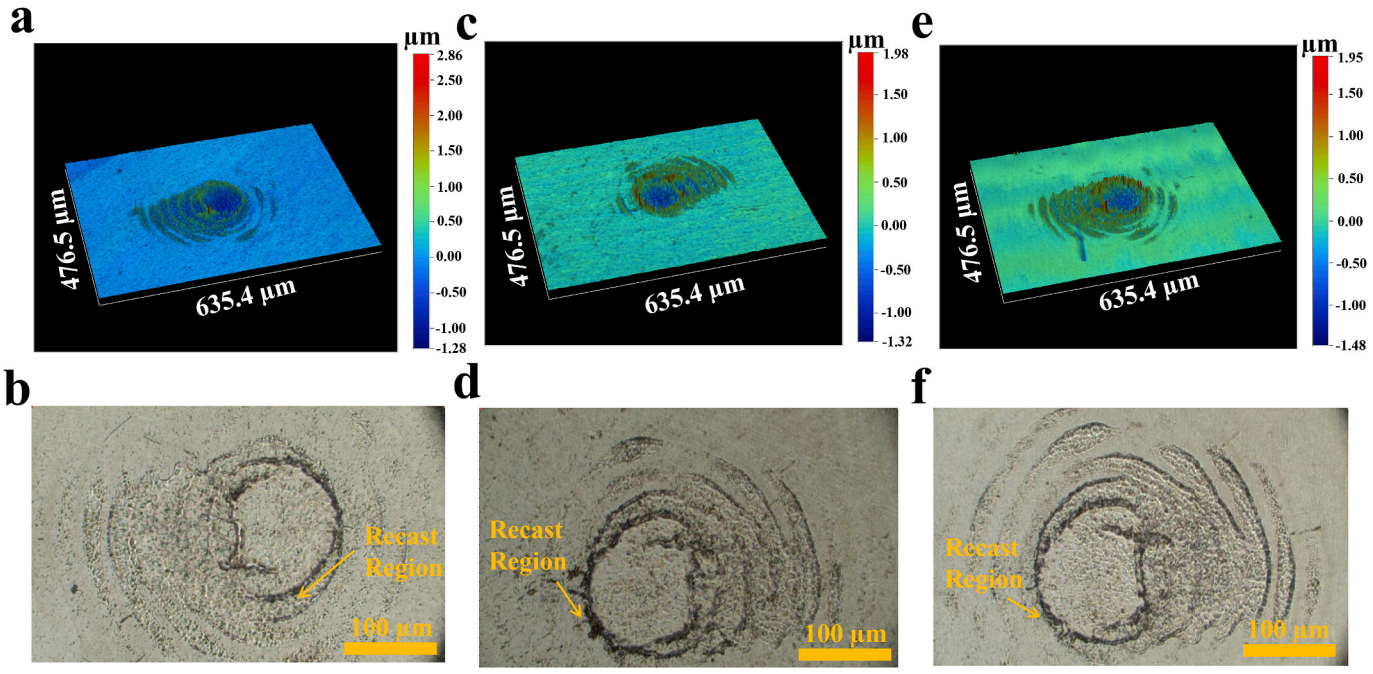


Fig. 3. Analysis of the surface pattern following a single pulsed laser exposure at 11.92 mJ (28802.67 J/cm^2), a, b)WLI and OM of the CoCuFeNiMnMo$_{0.5}$, c, d) WLI and OM of the CoCuFeNiMnMo$_{1.0}$, and e, f)WLI and OM of the CoCuFeNiMnMo$_{1.5}$.

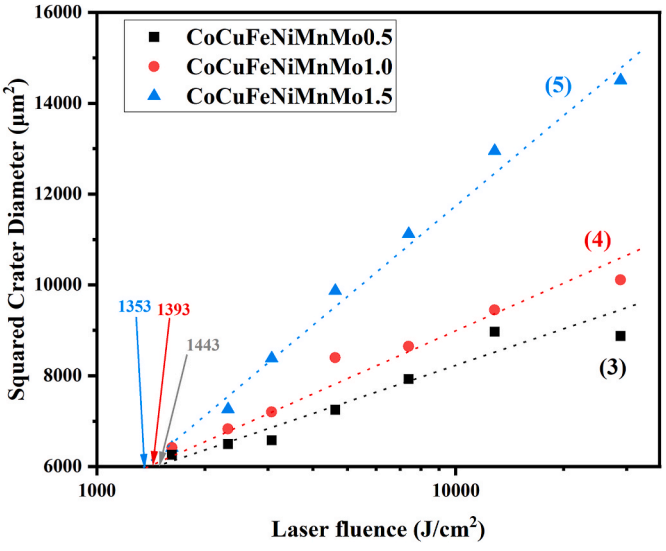


Fig. 4. The relation of craters diameters with increasing laser pulse energy on the CoCuFeNiMnMo$_x$ (x = 0.5, 1.0, and 1.5).

$$y = 0.3787\ log\ x - 1.0943 \quad R^2 = 0.9481 \tag{7}$$

$$y = 0.434\ log\ x - 1.2401 \quad R^2 = 0.9273 \tag{8}$$

Within this laser pulse energy range, all compositions of the HEA CoCuFeNiMnMo$_x$ (x = 0.5, 1.0, and 1.5) display a consistent linear slope. It's worth mentioning that the CoCuFeNiMnMo$_{1.5}$ composition exhibited the lowest ablation threshold at 0.14 mJ, while the highest threshold was observed for CoCuFeNiMnMo$_{0.5}$ at 0.23 mJ. This trend in ablation threshold aligns with the changes in Mo ratio, as reflected in crater diameter variations. Additionally, the ablation threshold values correlate with the mixing enthalpy, where CoCuFeNiMnMo$_{0.5}$, possessing the highest mixing enthalpy, exhibits the highest ablation threshold. Conversely, CoCuFeNiMnMo$_{1.5}$, characterized by the lowest mixing enthalpy, demonstrates the lowest ablation threshold. The rate of change in crater depth with increasing applied laser pulse energy for the three compositions of the HEA CoCuFeNiMnMo$_x$ (x = 0.5, 1.0, and 1.5) follows a similar trend, showing a dependence on the applied laser pulse energy. The CoCuFeNiMnMo$_{1.5}$ had the highest variation rate and CoCuFeNiMnMo$_{0.5}$ had the lowest variation rate. The increase in depth and the ratio of depth increment as a function of pulse energy, which is influenced by the incremental addition of Mo, exhibits a parallel trend

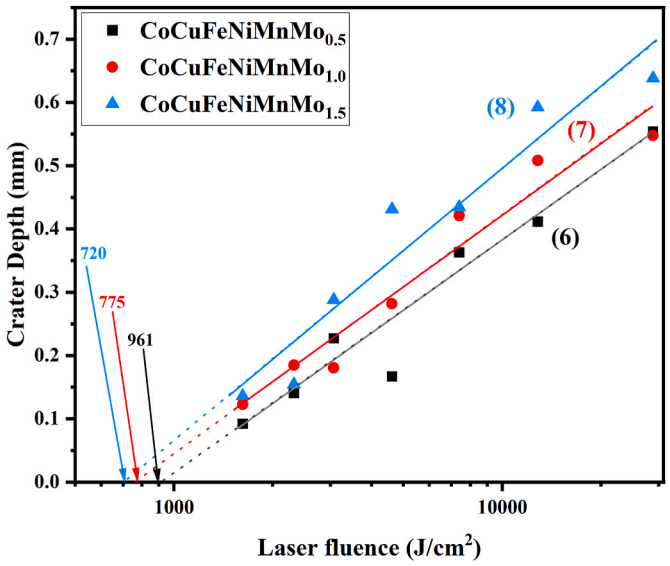


Fig. 5. The relation of craters depth increments with increasing laser pulse energy on the CoCuFeNiMnMo$_x$ (x = 0.5, 1.0, and 1.5).

with the expansion of crater diameter. This relationship is associated with the increasing pulse energy and the higher Mo content.

Fig. 6 presents the results of measurements investigating the effect of varying the number of laser pulses on crater depth. Fig. 6-a illustrates how different numbers of laser exposures (1, 10, 100, and 1000 pulses, represented by three separate columns with distinct colors) influence the crater depth in CoCuFeNiMnMo$_x$ (x = 0.5, 1.0, and 1.5) samples at an energy level of 11.92 mJ. The noticeable increase in depth as the number of exposures rises is evident, indicating a simultaneous increase in both crater diameter and depth. This observation aligns with the trends observed in the craters radius alteration with increasing the laser power shown in Fig. 4. Furthermore, it was observed that the crater depth increased with higher Mo content. For example, the depth of CoCuFeNiMnMo$_{0.5}$ increased from 0.23 μm after 1 pulse to 83.13 μm after 1000 pulses, reaching the lowest depth among the three samples with different Mo ratio. In contrast, the depth of CoCuFeNiMnMo$_{1.5}$ increased from 0.49 μm to 174.25 μm, representing the highest depth. This trend persisted across all pulse exposures, with depth differences increasing with the number of pulses. The disparities in depth between CoCuFeNiMnMo$_{0.5}$ and CoCuFeNiMnMo$_{1.5}$ were 0.26 μm, 1.3 μm, 2.11 μm, and 91.12 μm for 1, 10, 100, and 1000 pulses, respectively, with CoCuFeNiMnMo$_{1.5}$ exhibiting higher depth than CoCuFeNiMnMo$_{0.5}$. The depth profilometry of the crater after 1000 pulses for CoCuFeNiMnMo$_x$ (x = 0.5, 1.0, and 1.5) is shown in Fig. 6-b. The V-type groove of the craters after 1000 pulses is clearly shown, where CoCuFeNiMnMo$_{0.5}$ had the most shallow depth and CoCuFeNiMnMo$_{1.5}$ had the deepest. Examination of the edges of these V grooves reveals recast regions, characterized by small peak-like rises at the crater borders, which are detectable in profilometry graphs, such as those obtained from WLI (White Light Interferometry) analysis. The recast region is a predicted region of the crater when nanosecond laser are used (Takayama et al., 2018; Jing et al., 2023).

The laser ablation mechanism of CoCuFeNiMnMo$_x$ (x = 0.5, 1.0, and 1.5) alloys is predominantly governed by thermal processes induced by nanosecond laser pulses. When the alloy surface is exposed to high-intensity laser energy, rapid absorption occurs, leading to localized heating, melting, and vaporization of the material. The efficiency of this ablation process is significantly influenced by the thermophysical properties of the alloys, such as thermal conductivity, specific heat, and melting point, which dictate the rates of heat absorption, conduction, and dissipation. The observed crater features, including V-shaped grooves and recast layers, are indicative of rapid melting followed by re-solidification, underscoring the thermal nature of the ablation mechanism. The relationship between laser fluence and crater depth exhibits a quasi-linear dependence, where increased pulse energy results in greater material removal. Additionally, variations in Mo content impact the ablation threshold, with higher Mo-containing compositions demonstrating lower thresholds due to altered mixing enthalpy, which affects the alloy's capacity to endure laser-induced thermal stress. Overall, the interplay of thermal effects, alloy composition, and laser parameters dictates the observed ablation behavior in these HEAs.

4. Conclusion

In summary, the mixing enthalpy in HEAs plays a crucial role in determining the energetic interactions between dissimilar atoms, ultimately influencing the alloy's phase stability and properties. The laser ablation behavior of CoCuFeNiMnMo$_x$ (x = 0.5, 1.0, and 1.5) alloys is primarily driven by thermally induced processes from nanosecond laser pulses, where the efficiency of material removal is influenced by the alloys' thermophysical properties, laser fluence, and Mo content, with variations in these factors affecting heat retention, ablation threshold, and crater morphology through mechanisms of localized heating, melting, and re-solidification.

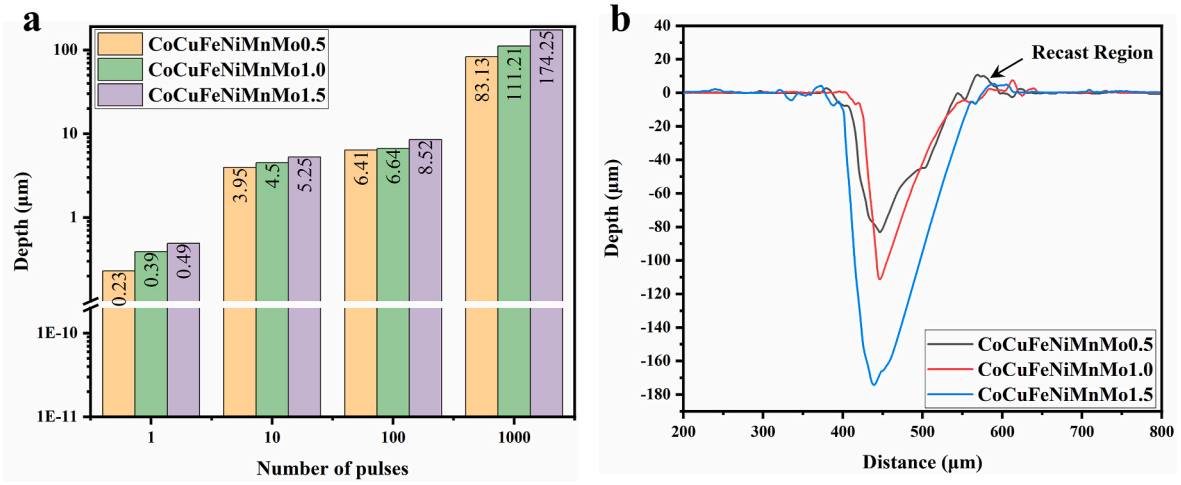


Fig. 6. The influence of the number of laser pulses on the depth of laser-exposed CoCuFeNiMnMo$_x$ (x = 0.5, 1.0, and 1.5) samples at 28802 J/cm^2 mJ a) The depth of the laser-induced craters after 1, 10, 100, and 1000 pulses and b) The depth profilometry of the crater after 1000 pulses.

The higher mixing enthalpy observed in $CoCuFeNiMnMo_{0.5}$ indicates stronger atomic bonds, while the lower mixing enthalpy in $CoCuFeNiMnMo_{1.5}$ suggests weaker atomic bonds relatively, potentially leading to reduced bond strength in the HEA. The calculated mixing enthalpy values for three compositions ($CoCuFeNiMnMo_{0.5}$, $CoCuFeNiMnMo_{1.0}$, and $CoCuFeNiMnMo_{1.5}$) further support this trend.

Moving on to the laser ablation study, the examination of $CoCuFeNiMnMo_x$ ($x = 0.5$, 1.0, and 1.5) HEAs under various laser powers revealed interesting trends. The laser-induced crater morphology exhibited a strong dependence on both the applied fluence and the number of laser pulses. Generally, an increase in laser pulse energy resulted in larger and deeper craters. The relationship between crater size and laser pulse energy followed a parabolic trend, with the rate of size increment decreasing as pulse energy increased.

Furthermore, the depth of the laser-induced craters showed a quasi-linear relationship on a logarithmic scale, with $CoCuFeNiMnMo_{1.5}$ exhibiting the lowest ablation threshold and the highest depth increment. The correlation between mixing enthalpy, Mo content, and ablation threshold suggests that the HEA with higher mixing enthalpy possesses a higher ablation threshold.

The investigation into the impact of the number of laser pulses on crater depth revealed a consistent increase in both diameter and depth with a higher number of exposures. $CoCuFeNiMnMo_{1.5}$ consistently exhibited greater depths compared to $CoCuFeNiMnMo_{0.5}$ across all pulse exposures, emphasizing the influence of Mo content on the laser ablation process.

CRediT authorship contribution statement

Hossein Mahdavi: Writing – review & editing, Writing – original draft, Investigation, Formal analysis, Data curation. **Abdullah Kepçeoğlu:** Writing – review & editing, Writing – original draft, Investigation, Formal analysis, Data curation, Conceptualization. **Armin Asghari Alamdari:** Writing – review & editing, Writing – original draft, Investigation, Formal analysis, Data curation. **Uğur Ünal:** Writing – review & editing, Writing – original draft, Investigation, Data curation. **Hadi Jahangiri:** Writing – review & editing, Writing – original draft, Visualization, Validation, Supervision, Resources, Methodology, Data curation, Conceptualization.

Ethical approval

Not applicable.

Funding

This research was generously funded by the TÜBİTAK 3501 CAREER Award under Project No. 122M937.

Declaration of competing interest

The authors declare that they have no known competing financial interests or personal relationships that could have appeared to influence the work reported in this paper.

Appendix A. Supplementary data

Supplementary data to this article can be found online at https://doi.org/10.1016/j.rsurfi.2025.100415.

Data availability

The data that support the findings of this study are available on request from the corresponding author, Dr. Hadi Jahangiri, hjahangiri@ku.edu.tr.

References

Asghari Alamdari, A., Jahangiri, H., Yagci, M.B., Igarashi, K., Matsumoto, H., Motallebzadeh, A., Unal, U., 2024. Exploring the role of Mo and Mn in improving the OER and HER performance of CoCuFeNi-based high-entropy alloys. ACS Appl. Energy Mater. 7, 2423–2435. https://doi.org/10.1021/acsaem.3c03227.

Assonov, S.S., de Groot, P.A., 2009. Chapter 6 - Oxygen. In: de Groot, P.A. (Ed.), B.T.-H. Of S.I.A.T. Elsevier, Amsterdam, pp. 405–618. https://doi.org/10.1016/B978-0-444-51115-7.00006-1.

Boulmer-Leborgne, C., Benzerga, R., Perrière, J., 2010. Nanoparticle Formation by femtosecond laser ablation. Springer Mater. Sci. 130, 125–140. https://doi.org/10.1007/978-3-642-03307-0_6.

Chen, W., Fu, Z., Fang, S., Xiao, H., Zhu, D., 2013. Alloying behavior, microstructure and mechanical properties in a FeNiCrCo0.3Al0.7 high entropy alloy. Mater. Des. 51, 854–860. https://doi.org/10.1016/j.matdes.2013.04.061.

Cropper, M.D., 2018. Thin films of AlCrFeCoNiCu high-entropy alloy by pulsed laser deposition. Appl. Surf. Sci. 455, 153–159. https://doi.org/10.1016/J.APSUSC.2018.05.172.

Gao, M.C., Yeh, J.-W., Liaw, P.K., Zhang, Y., 2016. Overview of High-Entropy Alloys. Springer Nature. https://doi.org/10.1007/978-3-319-27013-5_1.

Guo, S., Ng, C., Lu, J., Liu, C.T., 2011. Effect of valence electron concentration on stability of fcc or bcc phase in high entropy alloys. J. Appl. Phys. 109, 1–5. https://doi.org/10.1063/1.3587228.

Guo, H., Wang, X., Dupuy, A.D., Schoenung, J.M., Bowman, W.J., 2022. Growth of nanoporous high-entropy oxide thin films by pulsed laser deposition. J. Mater. Res. 37, 124–135. https://doi.org/10.1557/s43578-021-00473-2.

Ionin, A.A., Kudryashov, S.I., Samokhin, A.A., 2017. Material surface ablation produced by ultrashort laser pulses. Uspekhi Fiz. Nauk 187, 159–172. https://doi.org/10.3367/ufnr.2016.09.037974.

Jahangiri, H., Mohagheghi, S., Asghari Alamdari, A., Yilmaz, R., Gürcan Bayrak, K., Yu, F., Ghadbeigi, H., Ayas, E., Motallebzadeh, A., 2021. Microstructure development and mechanical performance of Al2CrFeMnTi light-weight high entropy alloy. Intermetallics 139, 107376. https://doi.org/10.1016/j.intermet.2021.107376.

Jahangiri, H., Morova, Y., Asghari Alamdari, A., Eroğlu, Z., Sennaroğlu, A., Guo, S., Metin, O., Motallebzadeh, A., 2023. Femtosecond laser-mediated preparation of HfNbTaTiZr refractory high-entropy alloy nanoparticles for photothermal therapy applications: influence of solvent and fluence. Intermetallics 156, 107834. https://doi.org/10.1016/j.intermet.2023.107834.

Jing, X., Wang, J., Lai, Z., Zheng, S., Husain Imran Jaffery, S., 2023. Thermal model for nanosecond laser ablation Al2O3 considering temperature dependence. Infrared Phys. Technol. 131, 104716. https://doi.org/10.1016/j.infrared.2023.104716.

Lednev, V.N., Filippov, M.N., Bunkin, A.F., Pershin, S.M., 2015. Laser ablation comparison by picosecond pulses train and nanosecond pulse. Laser Phys. Lett. 12, 126001. https://doi.org/10.1088/1612-2011/12/12/126001.

Lenzner, M., Krausz, F., Krüger, J., Kautek, W., 2000. Photoablation with sub-10 fs laser pulses. Appl. Surf. Sci. 154–155, 11–16. https://doi.org/10.1016/S0169-4332(99)00432-8.

Liu, J.M., 1982. Simple technique for measurements of pulsed Gaussian-beam spot sizes. Opt. Lett. 7, 196. https://doi.org/10.1364/OL.7.000196.

Liu, X., Du, D., Mourou, G., 1997. Laser ablation and micromachining with ultrashort laser pulses. IEEE J. Quant. Electron. 33, 1706–1716. https://doi.org/10.1109/3.631270.

Ma, D., Grabowski, B., Körmann, F., Neugebauer, J., Raabe, D., 2015. Ab initio thermodynamics of the CoCrFeMnNi high entropy alloy: importance of entropy contributions beyond the configurational one. Acta Mater. 100, 90–97. https://doi.org/10.1016/j.actamat.2015.08.050.

Mahdavi, H., Asghari Alamdari, A., Kepceoğlu, A., Yağcı, M.B., Ünal, U., Jahangiri, H., 2024. Optimization of laser-wavelength dependence for open-air atmospheric pressure pulsed laser deposition of AlCrFeMnTi high-entropy alloy for tailored surface properties. ACS Omega 9, 22495–22505. https://doi.org/10.1021/acsomega.4c03245.

Martínez-Carmona, M., Vallet-Regí, M., 2020. Advances in laser ablation synthesized silicon-based nanomaterials for the prevention of bacterial infection. Nanomaterials 10, 1–18. https://doi.org/10.3390/nano10081443.

Meghwal, A., Anupam, A., Murty, B.S., Berndt, C.C., Kottada, R.S., Ang, A.S.M., 2020. Thermal Spray High-Entropy Alloy Coatings: A Review. Springer US. https://doi.org/10.1007/s11666-020-01047-0.

Miracle, D.B., Senkov, O.N., 2017. A critical review of high entropy alloys and related concepts. Acta Mater. 122, 448–511. https://doi.org/10.1016/j.actamat.2016.08.081.

Mustafa, H., Pohl, R., Bor, T.C., Pathiraj, B., Matthews, D.T.A., Römer, G.R.B.E., 2018. Picosecond-pulsed laser ablation of zinc: crater morphology and comparison of methods to determine ablation threshold. Opt Express 26, 18664. https://doi.org/10.1364/OE.26.018664.

Mustafa, H., Mezera, M., Matthews, D.T.A., Römer, G.R.B.E., 2019. Effect of surface roughness on the ultrashort pulsed laser ablation fluence threshold of zinc and steel. Appl. Surf. Sci. 488, 10–21. https://doi.org/10.1016/j.apsusc.2019.05.066.

Pérez Blanes, H., Ghiasi, P., Sandkühler, J., Yesilcicek, Y., Pentzien, S., Conradi, A., Prinz, C., Al-Sabbagh, D., Thünemann, A.F., Ozcan, O., Witt, J., 2023. High CO2 reduction activity on AlCrCoCuFeNi multi-principal element alloy nanoparticle electrocatalysts prepared by means of pulsed laser ablation. J. Mater. Res. Technol. 24, 9434–9440. https://doi.org/10.1016/j.jmrt.2023.05.143.

Pickering, E.J., Jones, N.G., 2016. High-entropy alloys: a critical assessment of their founding principles and future prospects. Int. Mater. Rev. 61, 183–202. https://doi.org/10.1080/09506608.2016.1180020.

Preuss, S., Demchuk, A., Stuke, M., 1995. Sub-picosecond UV laser ablation of metals. Appl. Phys. A 61, 33–37. https://doi.org/10.1007/BF01538207.

Redka, D., Gadelmeier, C., Winter, J., Spellauge, M., Eulenkamp, C., Calta, P., Glatzel, U., Minár, J., Huber, H.P., 2021. Sub-picosecond single-pulse laser ablation of the CrMnFeCoNi high entropy alloy and comparison to stainless steel AISI 304. Appl. Surf. Sci. 544, 148839. https://doi.org/10.1016/j.apsusc.2020.148839.

Sharkov, B., Scrivens, R., 2005. Laser ion sources. IEEE Trans. Plasma Sci. 33, 1778–1785. https://doi.org/10.1109/TPS.2005.860080.

Shih, C., V Shugaev, M., Wu, C., V Zhigilei, L., 2020. The effect of pulse duration on nanoparticle generation in pulsed laser ablation in liquids: insights from large-scale atomistic simulations. Phys. Chem. Chem. Phys. 22, 7077–7099. https://doi.org/10.1039/D0CP00608D.

Song, D., Huang, X., Liu, Q., Li, G., Xu, X., Wang, X., Wang, J., Lu, X., Gao, F., 2024. Rational construction of ultrathin PtPdRhCuM (M=Mn, Co or Ni) high entropy alloy nanotubes with rich defects for enhanced electrochemical activity: electrochemical aldicarb sulfone sensing. Sensor. Actuator. B Chem. 405, 135337. https://doi.org/10.1016/j.snb.2024.135337.

Tahir, S., Shkodich, N., Eggert, B., Lill, J., Gatsa, O., Flimelová, M., Adabifiroozjaei, E., Bulgakova, N.M., Molina-Luna, L., Wende, H., Farle, M., V Bulgakov, A., Doñate-Buendía, C., Gökce, B., 2024. Synthesis of high entropy alloy nanoparticles by pulsed laser ablation in liquids: influence of target preparation on stoichiometry and productivity. ChemNanoMat 10, e202400064. https://doi.org/10.1002/cnma.202400064.

Takayama, N., Asaka, S., Yan, J., 2018. Nanosecond pulsed laser irradiation of sapphire for developing microstructures with deep V-shaped grooves. Precis. Eng. 52, 440–450. https://doi.org/10.1016/j.precisioneng.2018.02.008.

Wang, Y., Zhang, M., Huang, Y., Cao, X., Dong, Y., Zhao, J., Li, Y., Wang, Y., 2022. Ablation threshold modelling and validation of metal Nanosecond laser processing. Opt Commun. 523, 128608. https://doi.org/10.1016/j.optcom.2022.128608.

Yalçın, Ş., Örer, S., Turan, R., 2008. 2-D analysis of Ge implanted SiO2 surfaces by laser-induced breakdown spectroscopy. Spectrochim. Acta Part B At. Spectrosc. 63, 1130–1138. https://doi.org/10.1016/j.sab.2008.09.002.

Ye, Y.F., Wang, Q., Lu, J., Liu, C.T., Yang, Y., 2016. High-entropy alloy: challenges and prospects. Mater. Today 19, 349–362. https://doi.org/10.1016/j.mattod.2015.11.026.

Yeh, J.W., 2015. Physical metallurgy of high-entropy alloys. Jom 67, 2254–2261. https://doi.org/10.1007/s11837-015-1583-5.

Zhang, Y., Zuo, T.T., Tang, Z., Gao, M.C., Dahmen, K.A., Liaw, P.K., Lu, Z.P., 2014. Microstructures and properties of high-entropy alloys. Prog. Mater. Sci. 61, 1–93. https://doi.org/10.1016/j.pmatsci.2013.10.001.